Title

Conforming mesh modeling of multi-physics effect on residual stress in multi-layer powder bed fusion process

Permalink

https://escholarship.org/uc/item/5cs8k3f0

Authors

Kishore, Mysore Nagaraja

Qian, Dong

Soshi, Masakazu

et al.

Publication Date

2024-08-01

DOI

10.1016/j.jmapro.2024.06.033

Peer reviewed
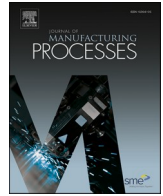
Conforming mesh modeling of multi-physics effect on residual stress in multi-layer powder bed fusion process

Mysore Nagaraja Kishore [a], Dong Qian [a], Masakazu Soshi [b], Wei Li [a,*]

[a] *Department of Mechanical Engineering, The University of Texas at Dallas, TX, USA*
[b] *Department of Mechanical and Aerospace Engineering, University of California Davis, CA, USA*

ARTICLE INFO

ABSTRACT

The current research aims to predict the residual stress accumulation and evolution in the powder bed fusion processed multi-layer thin wall structures through a conforming mesh modeling approach. It involves the discrete element method (DEM) interfaced with the volume of fluid (VOF) method using computational fluid dynamics (CFD) coupled with the finite element method (FEM). The conforming mesh approach developed in the research predicts multi-physics, its induced porosity, and the cumulative effect on the residual stress in the powder bed fusion processed Ti-6Al-4V thin wall structures. The results of the residual stress in the multi-layered component from this method were further quantitatively compared with the non-conforming finite element method. The results show the conforming mesh approach was not only effective in capturing the layer geometry, and defects induced during the printing, but also predicted the residual stress in the region of the defect more accurately than the non-conforming mesh methods.

1. Introduction

Powder bed fusion (PBF) is an additive manufacturing technology capable of printing three-dimensional geometry of complex shapes using micro-particles with unique microstructures and mechanical properties [1]. This bottom-up process is governed by the transient melting and solidification metallurgical mechanisms, which involve heat, mass, and momentum transfer induced by dynamic laser scanning [2]. Each layer can have an irregular melt pool track influenced by new layer powder consolidation, re-melting, and re-solidification phenomena. The PBF process is highly dynamic and transient. Due to this multiphysical nature, there are high chances of defects forming inside the layers for a variety of reasons [3].

For example, residual porosity forms due to insufficient melting of powders, and the low viscosity of melted metal powders. Rapidly solidified spherical features form and do not spread to create a homogeneous layer because surface tension can cause a balling effect which undermines the interlayer bonding, Also, the surface roughness at layer deposition due to the dimensions of the powder particles and their packing density can cause balling effects, humping, and other defects due to incongruent processing parameters [4]. So far, researchers have used different methods to simulate the single and multi-track PBF

process [5–7]. Apart from the computational models, researchers have developed a physics-based analytical model to calculate the residual stress in the direct metal deposition process and use an experimental approach to understand the residual stress in the layer deposition process [8–10]. Currently, there are three techniques widely used in macro-scale FEM models to capture the layer deposition process.

The first is called a "quiet" element method (QEM) in which the whole domain is discretized with FEM. The elements in the non-deposited layers are assigned with very low thermal properties until the deposited material reaches the region previously occupied by the quiet elements. The second is the "inactive" element method in which elements are added to the region to model the deposited material. Third, the "hybrid" method utilizes the "quiet" elements for the near-deposited region whereas the "interactive" elements are prescribed for the remaining non-deposited layers [11–14].

As shown in Fig. 1 and other types of FE methods, a major challenge is the lack of a good quality mesh to capture the shape of the deposited material. To address this, models that are based on the multiphysical CFD approach can predict the melt-pool evolution [15]. However, since CFD relies on the use of an Eulerian (spatial) grid, these methods need an accurate interface modeling technique to predict the shape of the printed layers and defects during multilayer, to track the history of residual
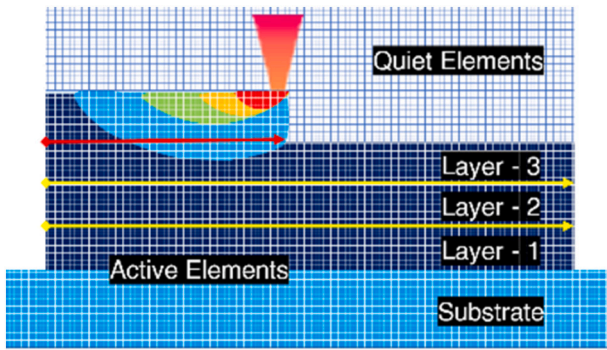
Fig. 1. Representation of quiet element-based finite element modeling of AM process.

stress, and more importantly, the surface and temperature history data transfer during each layer printing.

Given these critical limitations, a high fidelity, multi-scale, multi-physics comprehensive modeling framework is required for the multi-layer deposition of the PBF process. Instead of the pure Eulerian grid-based computational methodology, a mixed Eulerian-Lagrangian description can accurately capture the shape evolution of the deposited layers along with the porosity defects during the PBF process [16].

In this research, a computational fluid dynamics (CFD) model was established to simulate the powder bed fusion processed multi-layers. At first, it involves the volume of fluid (VOF) method to capture the fluid interface, solidification, and phase change. It further involves discrete element method (DEM) based powder particle packing and interaction. Second, the DEM-CFD-VOF model-based PBF layers were connected to finite element method-based thermomechanical analysis to study the residual stress. A novel interface technique adapted to this one-way coupling between CFD and FEM can transfer time-dependent temperature history along with its evolving surface morphology at each time step. Through benchmark example, the method was expected to capture the accumulation of the residual stress in multilayer printing with its surface roughness and defects. This one-way coupled CFD-FEM conforming mesh modeling technique was further compared with the existing FEM quiet element technique to show improvements in predicting surface morphology and its effect on residual stress prediction.

2. DEM-CFD-VOF-Interface-FEM methodology

The DEM model is composed of distinct spheres that can move independently and interact only when they meet each other. After

detecting the collision between two particles, e.g., particles 1 and 2 as shown in Fig. 2, an interaction is created wherein the normal stiffness (K_N) and tangential spring stiffness (K_T) properties are defined as

$$K_N = \frac{K_1 K_2}{K_1 + K_2} \text{ and } K_T = \frac{E_1 l_1 E_2 l_2}{E_1 l_1 + E_2 l_2} \tag{1}$$

in which the suffix 1 denotes particle 1 and the suffix 2 denotes particle 2, E is Young's modulus and l is the radius of particles. Each particle has 6 degrees of freedom (DOF) interacting cohesively and the representative DOFs of interacting particles.

Based on the two stiffnesses, normal and shear deformations are evaluated. Such kinematic variables of interaction are used to calculate the contact forces between the particles using constitutive law. The force/displacement form is considered in Eqs. (2)–(3) where F_N is the normal force, F_T is the shear force, normal and shear displacements are u_N, and u_T, F_T^t is the trial shear force, normal stiffness K_N, shear stiffness K_T and friction angle φ. These constitutive laws are in the form of non-cohesive elastic-frictional (φ) contact models.

$$F = F_N + F_T; F_N = K_N * u_N * n; F_T^t = K_T * u_T \tag{2}$$

$$F_T = \begin{cases} F_T^t * \dfrac{|F_N| \tan\varphi}{|F_T^t|} & \text{if } |F_T^t| > |F_N| \tan\varphi \\ F_T^t & \text{if otherwise} \end{cases}, \tag{3}$$

These constitutive laws are updated at each time step for all the colliding particles in the domain. The domain sample consists of n particles that have different particle distributions. These distributions form clusters called clumps and each clump contains either only two particles or multiple small particles. The left-out regions are considered void, and their fraction is calculated.

In the powder packing domain, the walls are considered as boundaries and the particles are filled. After filling, the particles can expand until the required packing distribution is obtained. The void ratio is calculated by Eq. (4).

$$e = \frac{\left[(b*h*t) - \sum_1^N \frac{4}{3}*\pi*r^3 \right]}{\sum_1^N \frac{4}{3}*\pi*r^3} \tag{4}$$

where b, h, and t are the dimensions of the sample domain, N is the total number of particles, and r is the radius of the spherical particle. Once the powder particles are settled on the top of the bed surface, the blade geometry is created as a moving object with a linear velocity of approximately 1–2 mm/s. This blade spreads the excessive powder
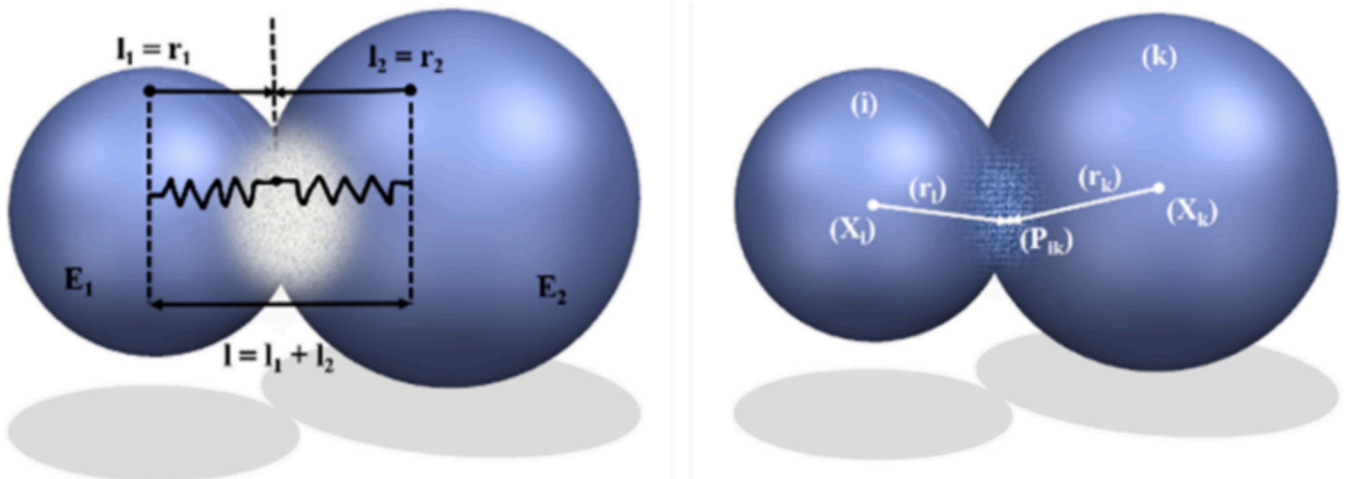

Fig. 2. Representation of powder particle interaction calculation in DEM.
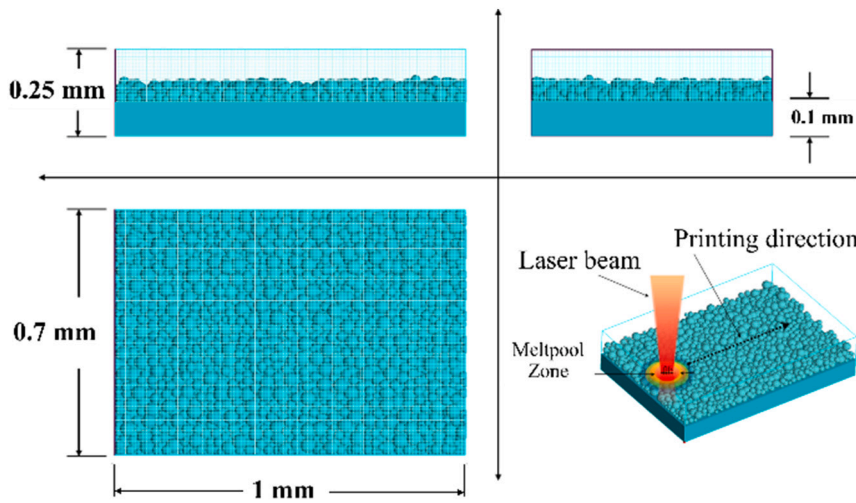
Fig. 3. CFD modeling domain of the PBF multi-layer simulation.

particles away from the surface.

The powder bed fusion process involves melt pool generation, layer formation, and the solidification of the layer. This highly transient process is solved using computational fluid dynamics (CFD) algorithms in the commercially available software FLOW-3D [17]. The CFD algorithm numerically solves the mass, momentum, and energy conservation equations with a finite volume approach [18,19]. The volume of fluid (VOF) technique is established for tracking and locating the fluid interfaces. In the CFD-VOF model as shown in Fig. 3, each grid is assigned a time-dependent fluid fraction step function F to define the fluid state. The function F with a value of 1 represents the state of fluid that exists fully, 0 represents the no-fluid, and in between represents the interface that must contain the free surface. It is governed by partial derivatives in the form of Eq. (5). which is further used to define the boundaries, where $\boldsymbol{v}$ is the velocity vector.

$$\frac{\partial F}{\partial t} + \nabla\cdot(\boldsymbol{v}\,F) = 0 \tag{5}$$

For each cell region, based on the information of F with its dependent variables such as velocities and pressures, conservations of momentum, energy, and mass Eqs. (6)–(8) are solved,

$$\frac{\partial \boldsymbol{v}}{\partial t} + (\boldsymbol{v}\cdot\nabla)\boldsymbol{v} = -\frac{1}{p}\nabla p + \mu\nabla^2\boldsymbol{v} + \boldsymbol{g} + \boldsymbol{f} \tag{6}$$

$$\frac{\partial h}{\partial t} + (\boldsymbol{v}\cdot\nabla)h = -\frac{1}{p}\nabla\cdot k\nabla T + \dot{q} \tag{7}$$

$$(\nabla\cdot\boldsymbol{v}) = 0 \tag{8}$$

where $\boldsymbol{f}$ is the force source, $\boldsymbol{g}$ is the acceleration due to gravity, μ represents the viscosity, h is the enthalpy, k is the thermal conductivity, and T is the temperature. The Gaussian heat source $\dot{q}$ is given by Eq. (9),

$$q(r) = \frac{\eta N P_{laser}}{\pi R^2} exp\left(-\frac{Nr^2}{R^2}\right) \tag{9}$$

where P_{laser} is the laser power, R is the laser radius, η is the absorptivity (or absorption rate) of the laser beam that depends on the laser wavelength and the material, N is the coefficient indicating the concentration of the laser energy within the beam radius, and r is the spot radius.

In addition, surface tension phenomena are included in the model to determine the molten pool surface. Except for common effects due to the Marangoni effect and buoyancy effect, the highly concentrated laser energy leads to the evaporation effect at the molten pool surface thereby creating an additional pressure exerted on the melt pool called recoil pressure. This acts as a major driving force on the molten pool surface and can be calculated by Eq. (10), where P_o is the atmospheric pressure, ΔH_v is the enthalpy change, T_v is the evaporation temperature, and R is the universal gas constant.

$$P_r = P_o exp\left(\frac{\Delta H_v}{R}\left(\frac{1}{T_v} - \frac{1}{T}\right)\right) \tag{10}$$

This evaporation phenomenon involves gaseous/fluid interface, heat transfer, and mass loss. This energy loss due to evaporation is determined by Eq. (11), where C_l is the specific heat of the fluid, T_l is the solidus temperature, and L_v is the latent heat of evaporation. The net loss of mass due to evaporation is given by Eq. (12), where R_{accom} is the accommodation constant, R is the universal gas constant, M is the molecular weight of the vapor, T is the average liquid temperature at the molten pool, P_v is the vaporization pressure and P_l^{sat} is the saturation pressure.

$$q_{loss} = C_l(T - T_l) + L_v \tag{11}$$

$$M_{net} = R_{accom} * \sqrt{\frac{M}{2\pi RT_{bdy}}} * \left(P_l^{sat} - P_v\right) \tag{12}$$

In the next step, an interface technique as shown in Fig. 4, an Eulerian-Lagrangian approach was developed to precisely mesh the complex geometries of the built component. In this implementation, a Lagrangian mesh is established based on the CFD-VOF simulations as shown in Fig. 4: First, the VOF method in the fluid solver provides detailed information on the surface profile of the deposited layer. These surface features will be represented by a surface triangular mesh (Standard Tessellation Language – STL format) that is commonly used for CAD (not to be confused with the FEM mesh introduced later).

Subsequently, the STL cad formatted deposited layer from the CFD analysis was used as a boundary inside the hexahedral mesh to be converted into 3D tetrahedral mesh. The 3D tetrahedral mesh size is dependent on the hexahedral mesh size which in turn has its size equivalent to the Eulerian grid size used in the CFD analysis. Once the Lagrangian mesh is constructed, the temperature values resolved at the center of the control volume in the thermal-fluid solver will be mapped to the FEM nodes using the standard FEM shape function interpolations. Compared with the existing quiet or inactive finite element methods, the proposed method significantly improves the accuracy of the surface representation and can also be extended to capture internal interfaces such as those due to porosity. These improvements will be demonstrated in numerical examples in the sequel.

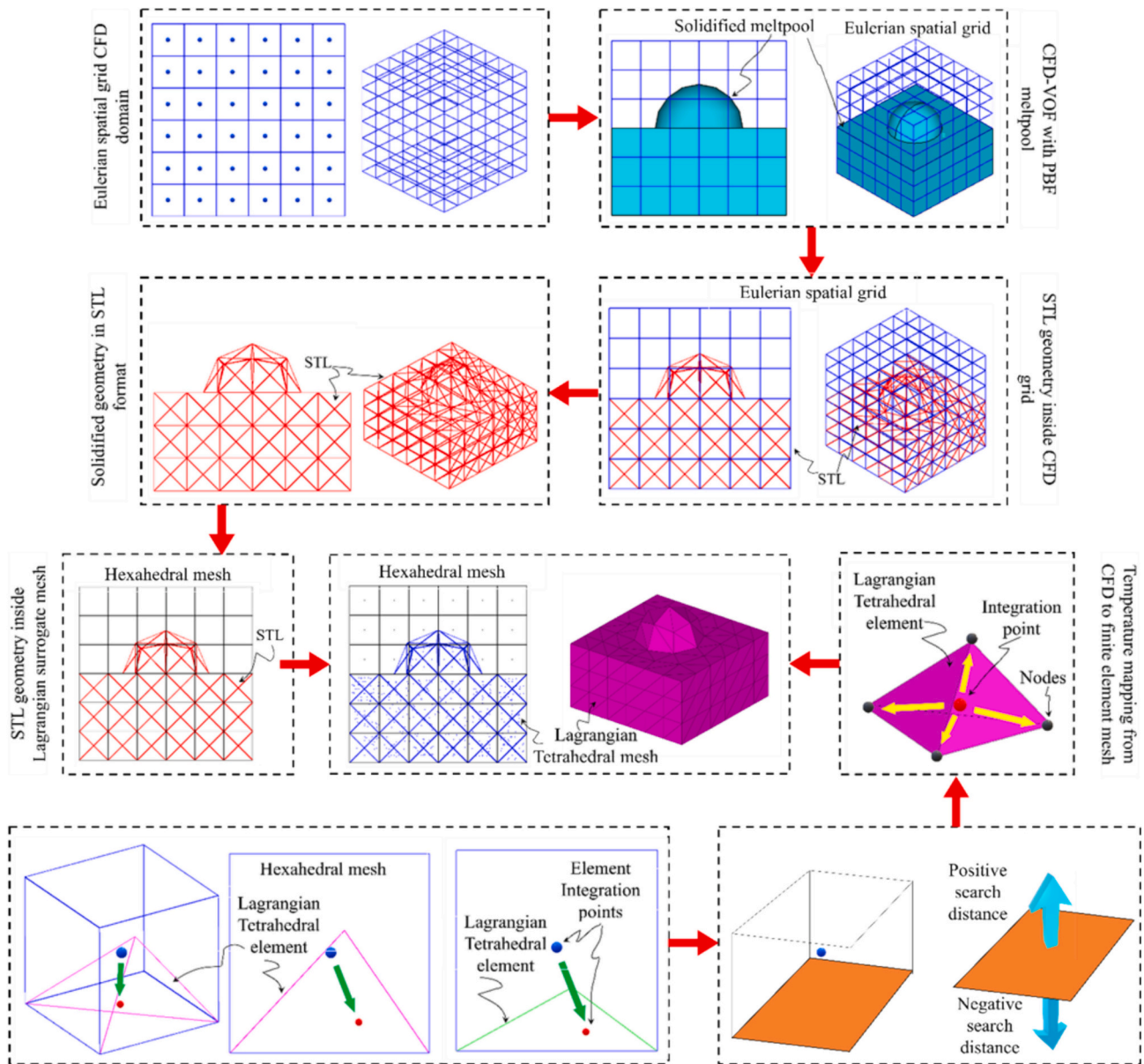The thermal-fluid simulation results are next transported to a

Fig. 4. The block diagram representing the one-way coupling framework between computational fluid dynamics simulation and finite element modeling. The framework uses fluid cell information on the temperature gradient, and the solidified fluid surface geometry.

thermal-mechanical model in ABAQUS [20] to calculate thermal stress at any given time in the L-PBF process. This thermomechanical model focuses on predicting residual stress and mechanical distortion. In the constitutive model, stress σ will be solved as a function of the total strain ε, given as $\sigma = \mathbf{C} : \varepsilon^e = \mathbf{C} : (\varepsilon - \varepsilon^T)$ with $\mathbf{C}$ being the elasticity matrix, ε^e, ε^T are respectively the elastic and thermal strains. A temperature and rate-dependent Johnson-Cook model is introduced in Eq. (13) to include the plasticity properties of the material.

$$k = \left(A + B\left(\varepsilon_{eff}^p\right)^n\right)\left(1 + Cln\left(\frac{\dot{\varepsilon}_{eff}}{\dot{\varepsilon}_0}\right)\right)\left(1 - \left[\frac{T - T_0}{T_m - T_0}\right]^m\right) \quad (13)$$

where k represents the effective stress, ε_{eff}^p is the effective plastic strain, $\dot{\varepsilon}_{eff}$ is the effective plastic strain rate, T is the temperature of the material, T_m is the melting point of the material, T_0 is the initial temperature, $\dot{\varepsilon}_0$ is the reference strain rate, and A, B, C, n, m are the material constants.

3. Ti-6Al-4V multi-layer printing case study

The PBF process simulation involves 150 W of power and a laser scanning speed of 1.6 m/s with the powder material of Ti-6Al-4V [21,22]. The simulation was subdivided into steps of powder consolidation, powder settling, powder spreading/layering, and melting. The first part of the simulation was the powder particle creation and settling. At first, a CFD-DEM domain was prescribed with a mesh grid size of 25 μm, in which 50,000 DEM particles were generated as one class or group during each layer printing. In this class of particles, three different species were considered. The first particle species consisted of powder particles that were 19 μm in diameter constituting 15 % concentration, the second particle species were 29 μm in diameter constituting 70 % in powder concentration and the third species of the particles were 43 μm in diameter constituting 15 % powder density concentration.

After printing the first layer, another 50,000 powder particles were modeled using DEM. Two layers of powder particles were formed on the base geometry. The 15 % concentration of the 19 μm diameter size

Table 1

The temperature-dependent material properties of the Ti-6Al-4V considered for the simulation.

Property	293 K	500 K	1000 K	1500 K	2000 K
Thermal conductivity $(\frac{W}{m-K})$	7.0	10.15	15.5	22.9	34.6
Specific heat $(\frac{J}{Kg-K})$	546	651	714	660	831
Coefficient of thermal expansion ($\times 10^{-6}$)	8.7	8.7	8.7	8.7	8.7
Density $(\frac{Kg}{m^3})$	4420	4366	4309	4240	3886

Table 2

Johnson-Cook model parameters of Ti-6Al-4V [23].

| A	B	n	m	C
1098 MPa	1092 MPa	0.93	1.1	0.014

powder particles was effective in filling the gap between the larger particles. This was essential to avoid any probable defects during the melting process. The maximum powder-packed center region was chosen for the deposition. The laser spot radius was set at 50 μm and the laser focal distance was set at 2.5 mm. This modeling approach can be extended to build any number of additional layers.

3.1. Thermomechanical properties of Ti-6Al-4V

The model consists of a laser heat source model with a laser path. The CFD-VOF domain as shown in Fig. 3 was divided into two regions. The fluid region's top domain is air, and the bottom domain region is the substrate. The deposition happens in the fluid region with air. These two regions have meshed with a grid size of $200\mu m$. The substrate domain size was $1.5^{''} \times 0.5^{''} \times 0.25^{''}$. The walls were modeled with symmetric boundary conditions with PBF working temperatures and convective heat transfer conditions, and the Z-axis was provided with atmospheric pressure conditions. Then the full domain was assigned with temperature-dependent fluid and thermal properties. The temperature-dependent viscosity ranges from $0.0032 \, Pa-s$ at 1650 K to $0.0024 \, Pa-s$ at 1900 K, and the constant latent heat of fusion of $286 \frac{kJ}{Kg}$ was used in the simulation. Some of these thermofluidic material properties are summarized in Table 1.

Further, the temperature and rate-dependent Johnson-Cook model using Eq. (13) and Table 2 was implemented to compute the plastic strain.
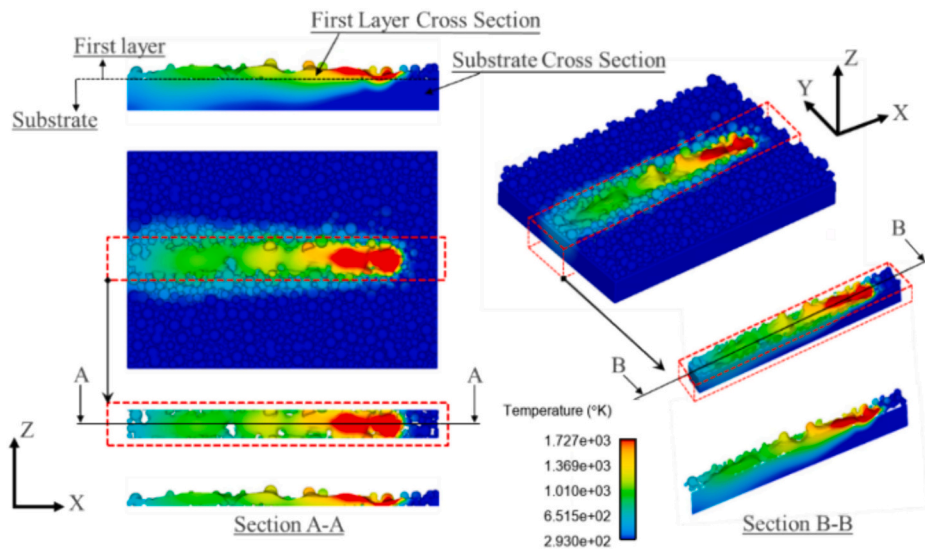
Fig. 5. The CFD-VOF simulation of the PBF processed the first layer of the single track Ti-6Al-4V depicting the temperature distribution.
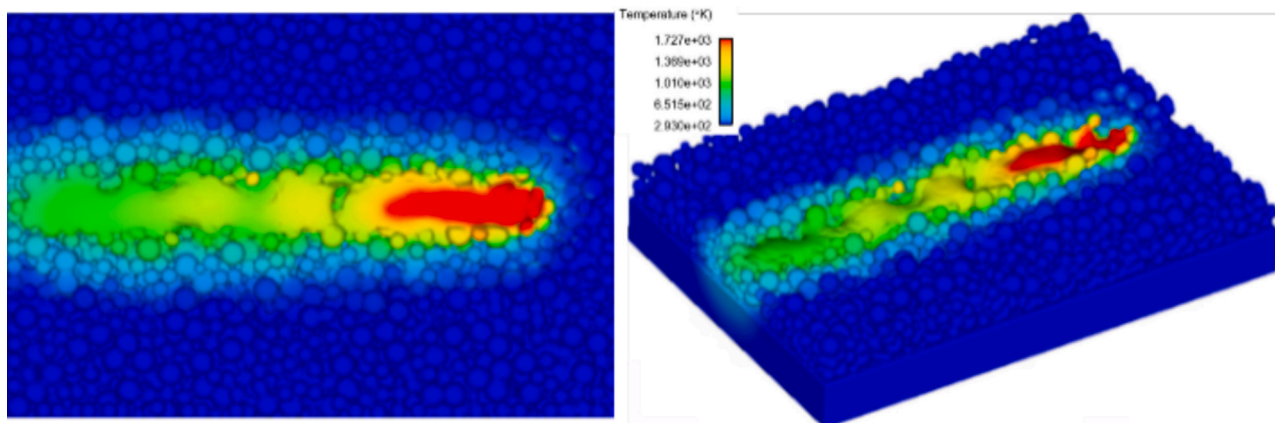
Fig. 6. The CFD-VOF simulation of the PBF processed the second layer of the single track Ti-6Al-4V depicting the temperature distribution.
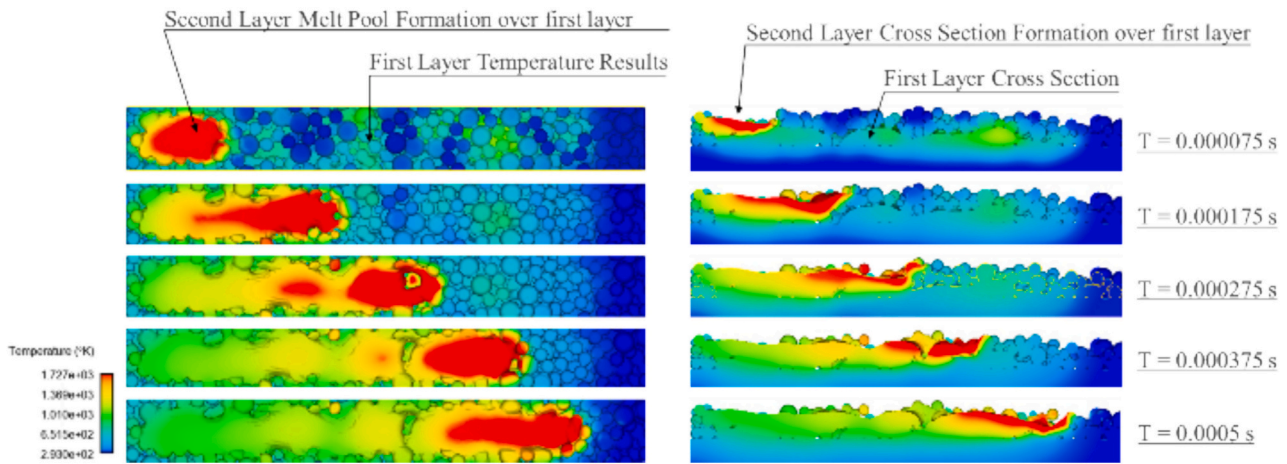
Fig. 7. The temperature distribution of the second layer over the first layer depicting the cross-section and top view implying the continuity of the CFD-VOF simulation of the multi-layer printing. The simulation also depicts the remelting of the first layer and semi-melted powders for the second layer before layer movement.
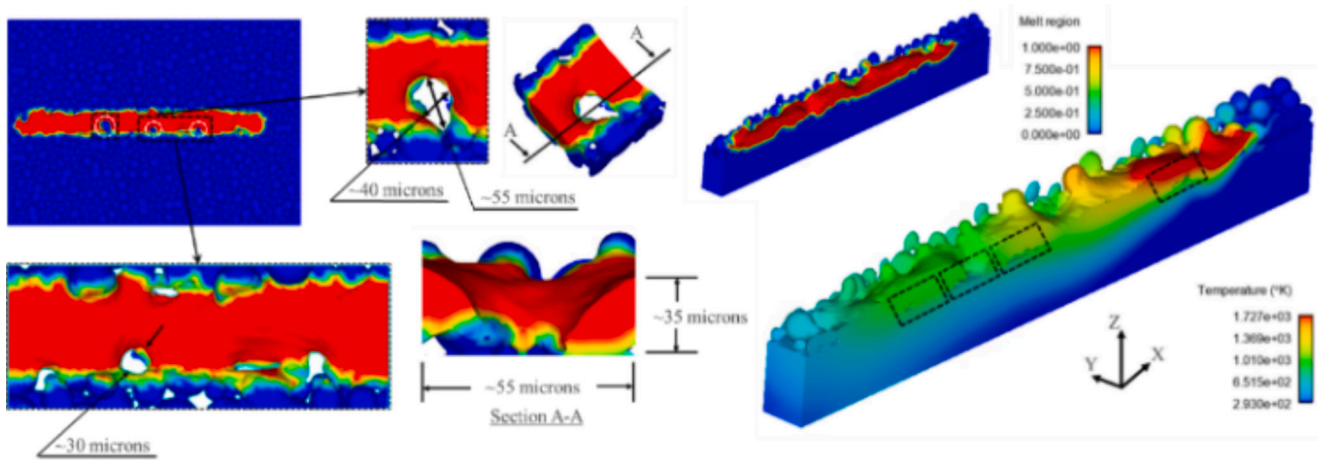

Fig. 8. The porosity formation across the printed domain during first layer printing depicting small pores at the periphery of the printing due to semi-melted powders. The melt region red implies fluid melted, and blue implies the un-melted region. (For interpretation of the references to color in this figure legend, the reader is referred to the web version of this article.)
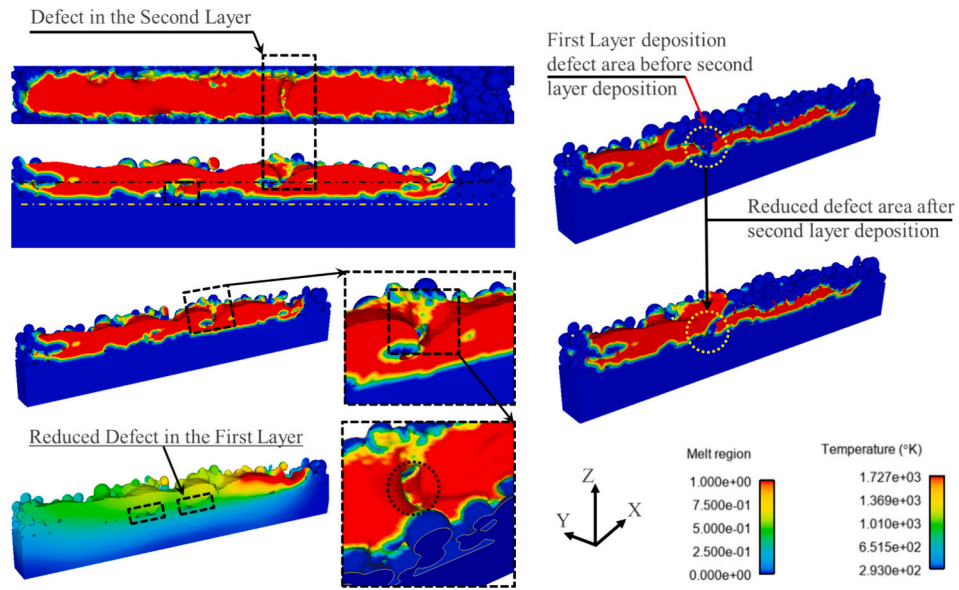
4. Results

4.1. Multi-layer PBF processed Ti-6Al-4V

The simulation plays a major role in analyzing the transient temperature distribution because it is very difficult to measure the temperature profile in the experiment. Figs. 5 and 6 show the transient temperature distribution of the first layer and second layer, respectively. The Ti-6Al-4V alloy has a solidus temperature of 1600 K and a liquidus temperature of 1650 K. These temperature limits have been exceeded by several hundred degrees in the melt pool region. The highest temperature is at the melt pool region at the time of melting. This high-temperature gradient further causes a surface tension gradient in the melt pool region that generates a Marangoni flow.

The temperature gradient along with the solidification growth phenomenon affects the surface morphology and the cooling rate affects the microstructure of the formed layers. During the deposition of the second layer, the heat transfer from the molten pool is directed downwards to the substrate through conduction. Also, across the surface of the melt pool, the temperature distribution is progressively elongated away from the distance of the laser beam where it has a highly concentrated band (red region).

In the CFD-VOF model, the surface roughness of the PBF layer can be precisely simulated. In the numerical example, during the deposition of the first layer in Fig. 5, at two regions, the spatters landed on the melt pool deposition, and two small cavities (approximately 28 μm in diameter) followed by a relatively large cavity (approximately 45 μm × 51 μm area, and 40 μm in depth) was formed (Fig. 8). One of the main reasons for this cavity formation is the dynamic melt pool region and partially melted powder particles. These cavities and spatters affect the surface roughness followed by irregular solidification growth. Once the second layer is formed in Fig. 7, the large cavity was partially filled, and the surface was relatively smoothened with a uniform thickness of 30 μm.

The formation and evolution of the defects depend on the operating parameters such as laser power, scanning speed, and particle size distribution. It can be observed that when the molten pool is continuous as observed in the second layer (Fig. 9), there was no defect occurrence such as balling effect, and porosity. One reason for the smooth molten pool flow is the particle size distribution. In this simulation, three different particle size distributions were considered, and the smallest (19 μm) particles are packed more along with the second layer melt pool region compared to that of the first layer. These particles melt completely for the given laser power and the laser scanning speed

Fig. 9. The porosity formation across the printed domain during second-layer printing. The simulation results depict the evolution of the larger pores from the first layer, trapped pores after the second layer melts, and new small pores formation. The melt region red implies fluid melted, and blue implies the un-melted region. (For interpretation of the references to color in this figure legend, the reader is referred to the web version of this article.)
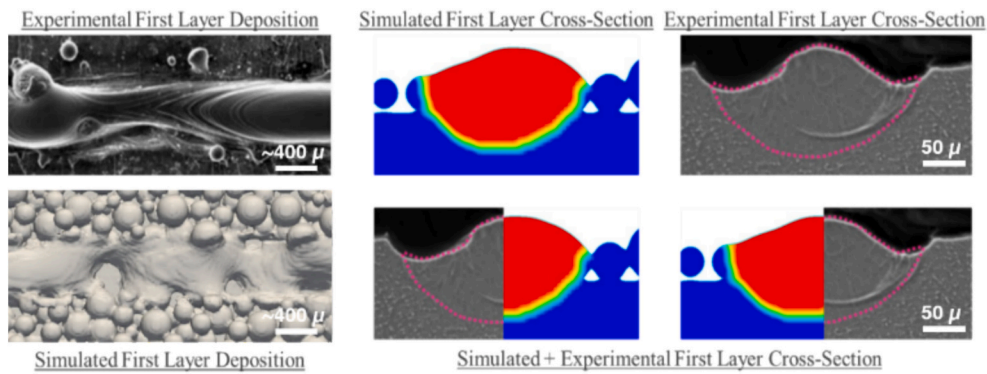
Fig. 10. Reference experimental validation of the meltpool cross-section of the single layer Ti-6Al-4V with the simulated meltpool cross-section.
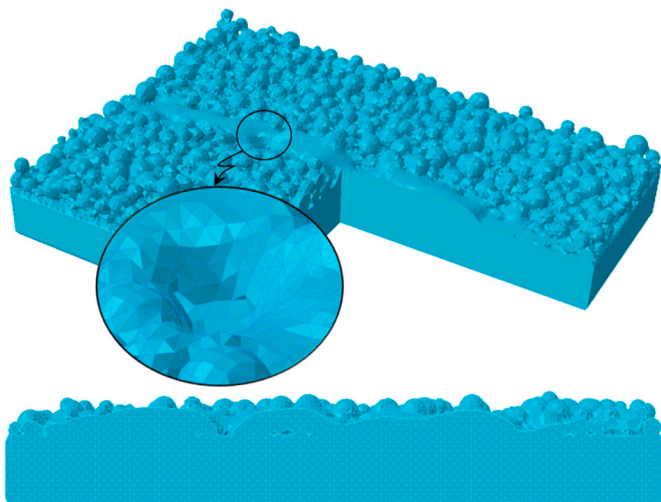
Fig. 11. Novel interface method resulted in finite element tetrahedron mesh model of the first layer of the PBF processed Ti-6Al-4V.
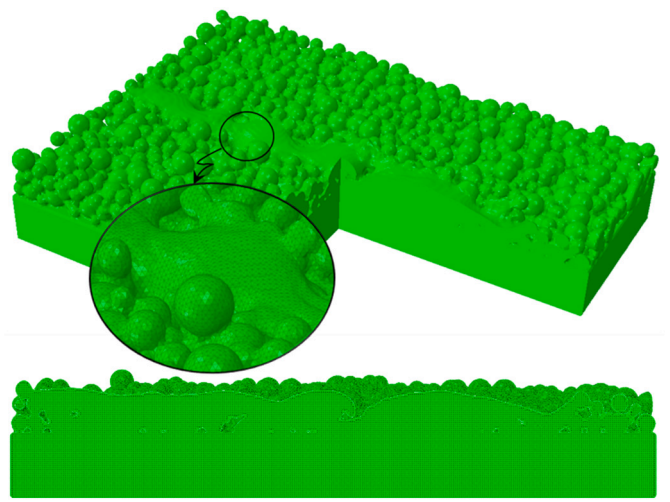
Fig. 12. Novel interface method resulted in finite element tetrahedron mesh model of the second layer of the PBF processed Ti-6Al-4V.
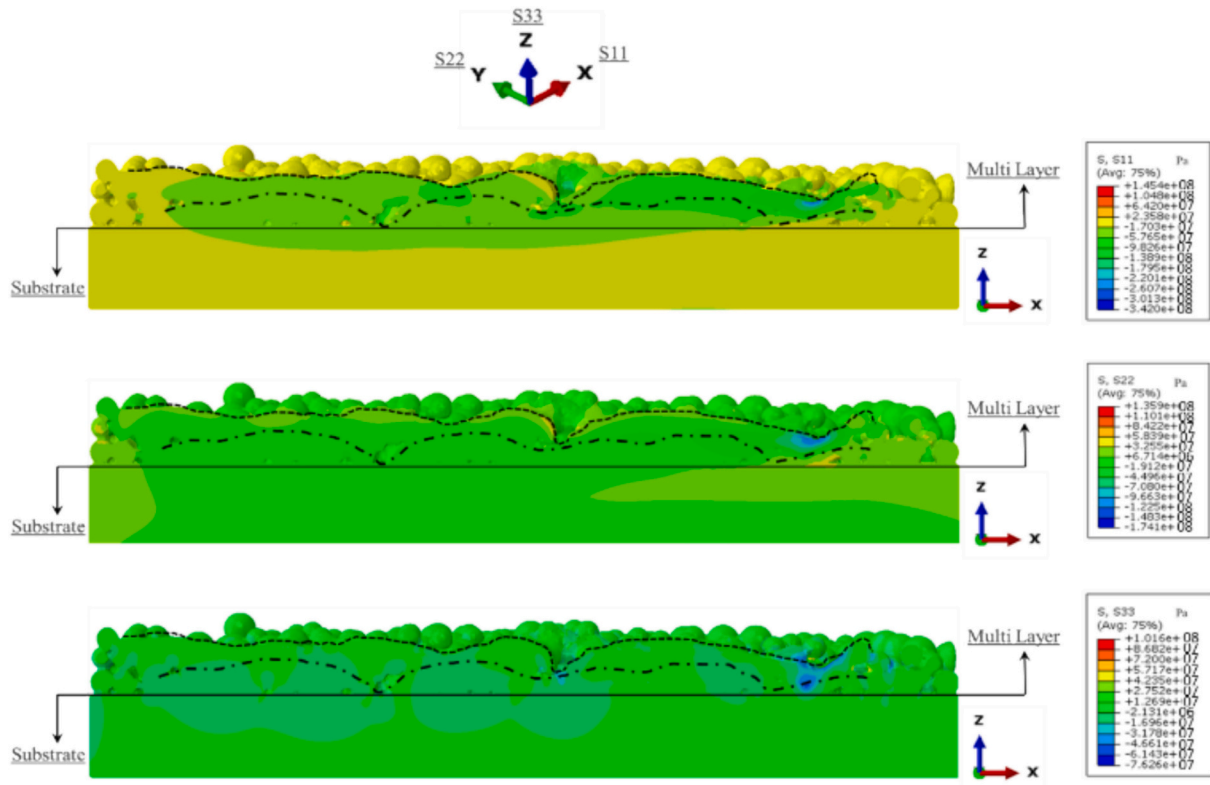
Fig. 13. Normal residual stresses depicting tensile and compressive residual stresses at the PBF-processed multi-layer thin walls at the mid-length cross-section.
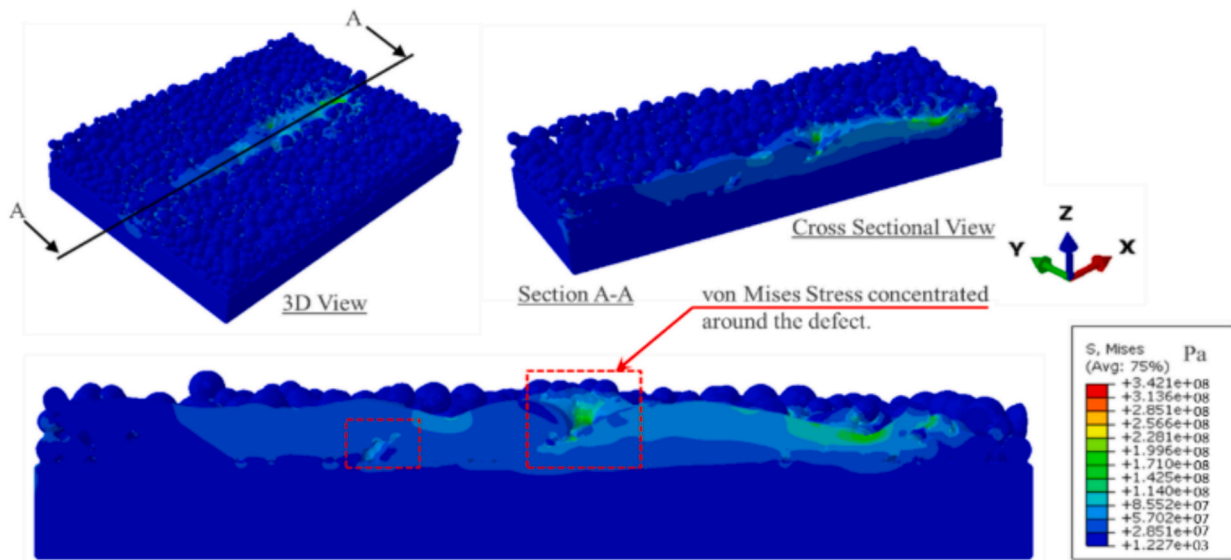

Fig. 14. Von Mises residual stress due to temperature gradient in the PBF simulation depicting the critical regions with defects causing significant residual stress concentration.

compared to that of 43 μm powder particles. This helps in reducing the surface roughness and avoids corrugated edges. Even though this work does not study the effects of different scanning speeds, laser powers, and powder particle distributions, the developed computational approach for the multi-layer PBF process can verify all these operating parameters effectively. It helps in understanding the evolution of the defects from the start of the first layer to the end of the second layer.

After the first layer was deposited, its geometric characteristics were validated with the experimental observations from the reference [24]. In

Fig. 10, the shape of the molten pool predicted by the multiphysics model is compared to the experimentally observed molten pool, where the red color indicates the simulated molten region, while the blue color indicates the unmelted region in the powder bed. Due to specific manufacturing features of PBF (interaction between laser beam and metallic powder bed, fast scanning speed, and laser power, etc), the width of the single track was not uniform, and some un-melted particles adhered to the single-track region. The laser parameters considered in the simulation and the experiment are the same. This comparison shows
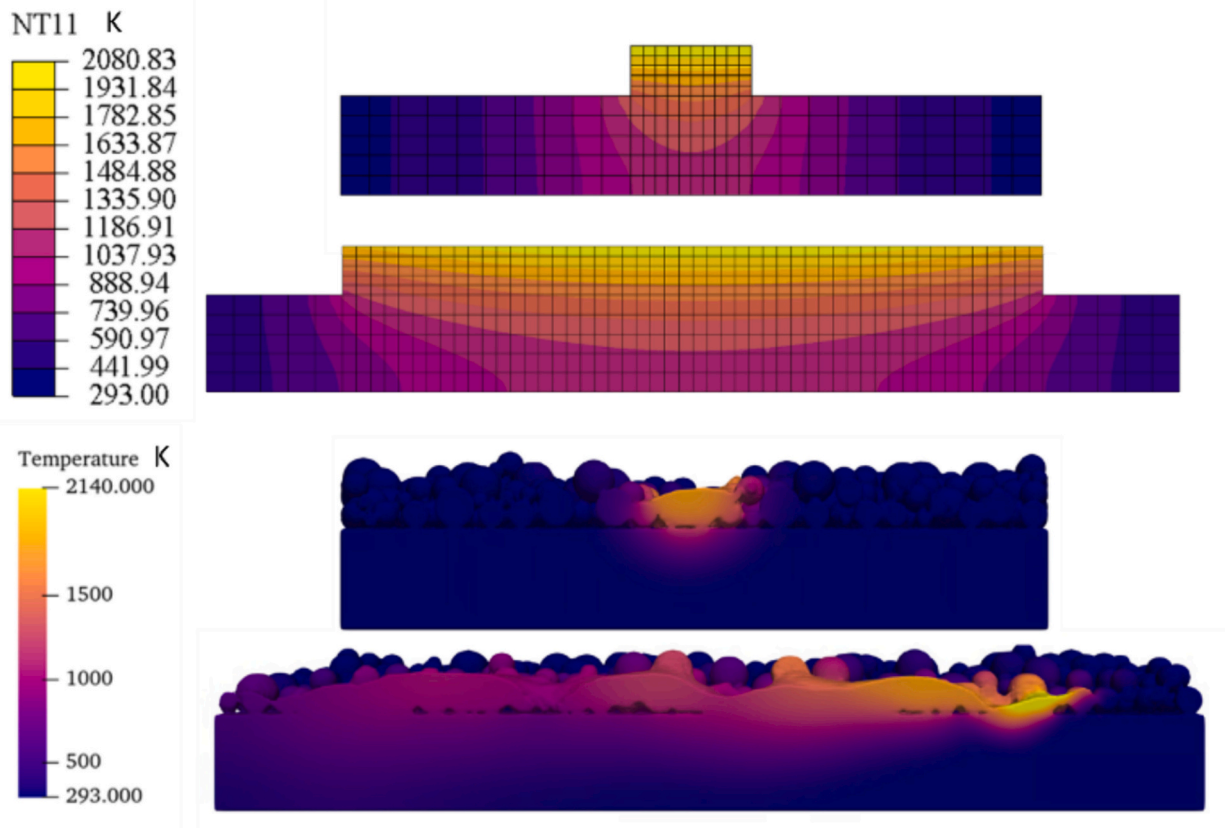
Fig. 15. The temperature distribution comparison between the quiet element approach (top) and the CFD-FEM coupling (bottom) of the PBF-processed single layer.
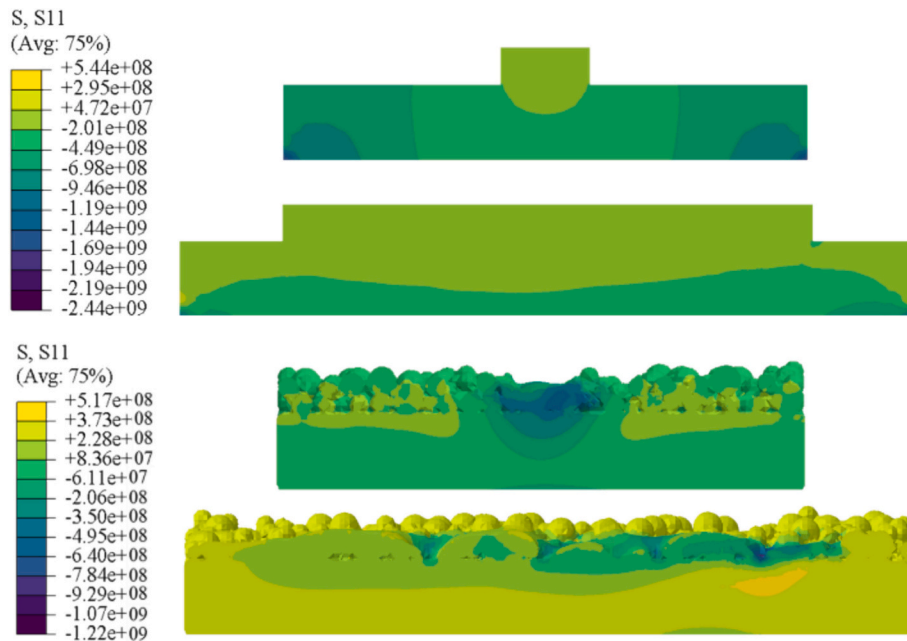

Fig. 16. Normal stress in the printing direction {S11 (Pa)} depicting the FEM-only method at the top and the CFD-FEM coupling method at the bottom.

that the predictions from the multiphysics model agree well with the experimental observation.

4.2. Residual stress prediction of multi-layer PBF processed Ti-6Al-4V

The apparent consequences of the defects, transient thermal behavior, and dynamic melt pool region discussed in the previous sections are the steep temperature gradient, thermal strains, and residual stress. These directly affect the quality of the component and can cause a wide range of distortions, geometrical instabilities, and failures related to delamination, fatigue, and fracture. These drive the qualitative analysis requirement of the PBF-manufactured components in real-life
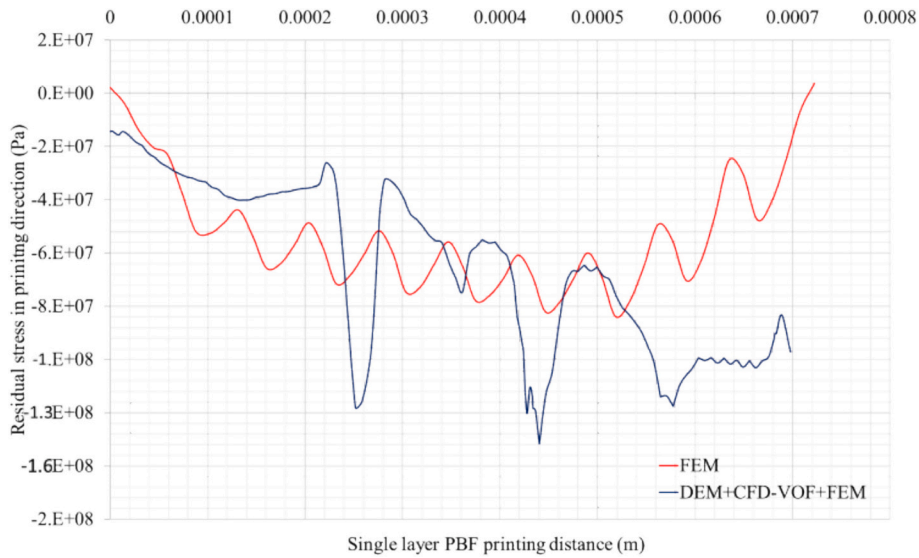
Fig. 17. Normal stress in the printing direction {S11 (Pa)} highlighting peak stress concentrations predicted by the CFD-FEM coupling method.
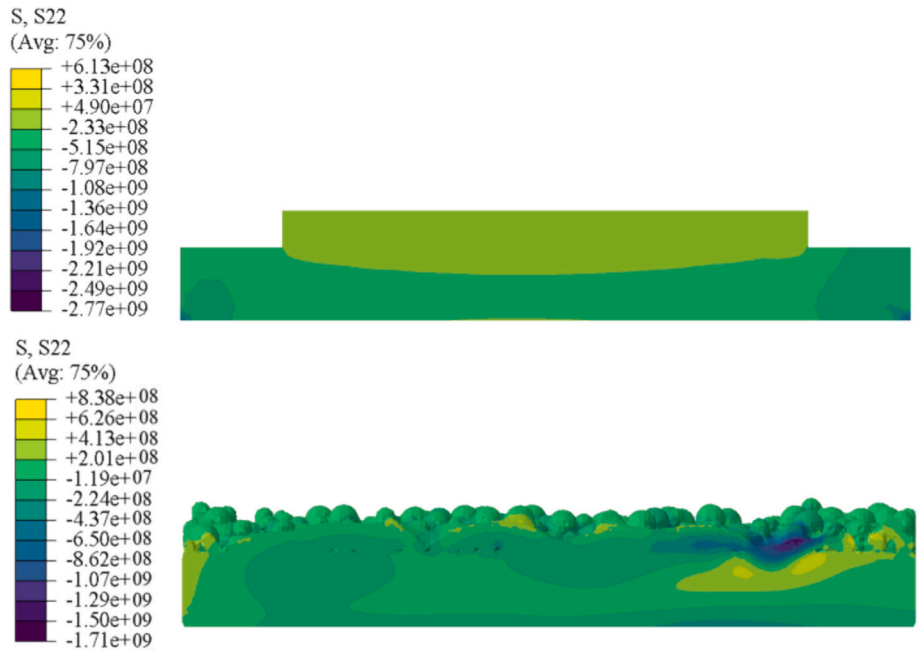

Fig. 18. Normal stress in the transverse to printing direction {S22 (Pa)} depicting the FEM-only method at the top and the CFD-FEM coupling method at the bottom.

applications. Hence, quantification of the accumulation of the residual stress due to steep temperature gradient at the macro level is essential before qualifying the component for usage. It helps in deciding the operative capabilities of the PBF-manufactured components in real-life applications.

Like in every other AM process, PBF has high cyclic heating, solidification, and build time which leads to residual stress formation within the component. The root cause is the rapid thermal expansion and contraction which are highly transient. Their magnitudes depend on the surface geometry, layer deposition, temperature-dependent material properties, and operating parameters. To study the residual stress in the layers deposited, the CFD model was integrated with the FEM model, and the FEM mesh is shown in Figs. 11 and 12.

In FEM analysis, the temperature-dependent mechanical properties were used to compute the residual stress and thermal strains. Figs. 13 and 14 show the distribution of the residual stress in three principal

directions that are deposition direction, transverse to deposition direction, and thickness direction, respectively, and the von Mises stresses. In the first layer, the maximum normal stress is in the transverse direction (σ_{yy}) at the surface of the deposition, and the nature of residual stress is tensile. This was also observed in the layer's thickness direction and towards the end of the layer deposition, a steep compressive stress region is observed. The magnitude of the stress will change during the cooling stage, and the temperature field at the last time step is considered for the current stress analysis.

This high-stress region on the surface of the first layer was relieved partially due to the reheating and cooling effects of the second layer deposition. The maximum stress accumulation is found at the top surface of the second layer. At the interface between the two layers, the stresses slowly shift from high tensile to low compressive. Finally, the residual stress in the thickness direction is compressive at the center of the first and second layers and tensile at the periphery. These stresses are
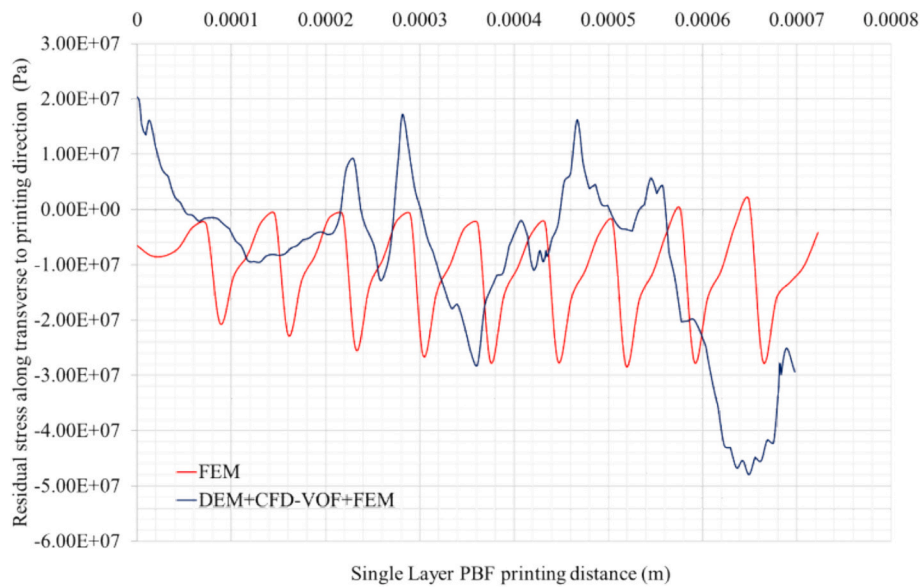
Fig. 19. Normal stress in the transverse to printing direction {S22 (Pa)} highlighting peak stress concentrations predicted by CFD-FEM coupling method.

highly non-uniform at the defect regions of the interface between the layers and the interface between the layer and the substrate.

5. Discussion

5.1. Conforming mesh v/s non-conforming mesh method

To verify the accuracy of the novel interface-based CFD-FEM coupled thermomechanical simulation, another comparison case study was conducted with a quiet element approach using the finite element method. The single-layer FEM-only simulation was compared with CFD-FEM coupled simulation for residual stress at the mid-length cross-section of the layer at the surface. A moving heat source based on the same power and scanning speed used in the CFD simulation was used to simulate thermal distribution. Following thermal analysis, the temperature distribution was used to simulate thermal residual stresses.

Fig. 15 depicts the temperature distribution at the last time step of the single-layer deposition. The advantage of the CFD-VOF method was that it distinguishes the meltpool zone, heat-affected zone, and solidification zone. The FEM, on the other hand, distinguishes these zones during the deposition, but with non-conforming geometry. Both methods can effectively predict the temperature gradient in the meltpool zone. However, during the cooling stage, the heat transfer in the FEM method distributes to the entire geometry very rapidly whereas the CFD-VOF method predicts the heat transfer from the meltpool zone to the rest of the geometry accurately.

The temperature gradient in the FEM thermal analysis was further used for the mechanical analysis to visualize the thermal residual stresses in the first layer. The residual stress was measured at the surface nodal locations at the mid-length cross-section of the first layer printed. Fig. 16 describes the residual stress component along the printing direction. The top contour represents the finite element method, and the bottom contour represents the CFD-FEM coupling method. The FEM predicted near uniform low-range compressive residual stress whereas CFD-VOF showed the concentration of tensile and compressive stresses.

Fig. 17 represents the residual stress differences along the printing direction to the length of the first layer. The FEM predicted a compressive stress range -45 MPa to -65 MPa mid-section, and 10 MPa to -40 MPa at the ends. The CFD-FEM coupling method results in -40 MPa to -80 MPa on average in the mid-section with two exceptions of -100 MPa and -150 MPa at two different locations. These locations are where stresses are more concentrated at the defect regions. At the end of

printing, due to the dip in the powder melting region, the residual stresses were further concentrated. Whereas the FEM did not show these concentrations and due to uniform elements and material presence, the stresses were diverging towards tensile residual stress.

Like the S11 normal stress component, the transverse component S22 normal stress in the finite element method (Fig. 18) shows a uniform distribution of the compressive residual stress ranging from ~0.5 MPa to -25 MPa. Whereas in the coupling method, the distribution shows peaks in tensile and compressive regions (Fig. 19). The overall residual stress trend correlates with the FEM method with average stress within the FEM method results range. However, the peaks are beyond the FEM results range representing the defect regions in the CFD simulation as shown in the contours from the figure. These stress concentration peaks are more tensile around the defects which needs to be alleviated. Overall, the CFD-FEM coupling method can effectively predict these peaks and their causes which are usually defects formation during printing.

6. Conclusion

A coupled multi-scale and multiphysics framework is developed to analyze the multi-layer deposition of the PBF process and demonstrated with Ti6Al4V alloy. It is shown that the computational approach accurately captures the formation of defects like porosity. The framework provides a tool for analyzing the effect of these defects on the processing conditions such as laser parameters, deposition strategy, and powder packing distribution.

This high-fidelity model can be extended to the simulation of the deposition of many layers in a continuous process that resembles the actual PBF process in applications. Such multi-layer simulations are required to understand the evolution of the defects, the dynamic nature of the melt pool region, the transient temperature gradient, and its evolution beyond the interface from one layer to another. This method effectively predicts the evolution of the defects between successive layers and provides a detailed understanding of the multi-layer melt pool characteristics. The inclusion of particle dynamics, laser beam characteristics, and transient melt pool region physical phenomena, followed by interfacing with the macro-level FEM to determine the residual stress can provide a complete overview from physics to process and from mesoscale to macro-scale. It is possible to extend the computational tools to optimize the process parameters that also allow the prediction of surface morphology changes.

CRediT authorship contribution statement

Mysore Nagaraja Kishore: Conceptualization, Data curation, Formal analysis, Investigation, Methodology, Visualization, Writing – original draft. **Dong Qian:** Project administration, Resources, Supervision. **Masakazu Soshi:** Investigation, Supervision, Writing – review & editing. **Wei Li:** Conceptualization, Investigation, Project administration, Resources, Supervision, Writing – original draft, Writing – review & editing.

Declaration of competing interest

The authors declare that they have no known competing financial interests or personal relationships that could have appeared to influence the work reported in this paper.

Data availability

The raw/processed data required to reproduce these findings can be provided upon request.

References

[1] Li W, Kishore MN, Zhang R, Bian N, Lu H, Li Y, et al. Comprehensive studies of SS316L/IN718 functionally gradient material fabricated with directed energy deposition: multi-physics & multi-materials modelling and experimental validation. Addit Manuf 2023;61. https://doi.org/10.1016/j.addma.2022.103358.

[2] Li W, Nagaraja KM, Zhang X, Zhou R, Qian D, Lu H. Multi-physics modeling of powder bed fusion process and thermal stress near porosity. Manuf Lett 2022;31: 78–82. https://doi.org/10.1016/j.mfglet.2021.07.012.

[3] Li J, Shi W, Lin Y, Li J, Liu S, Liu B. Comparative study on MQL milling and hole making processes for laser beam powder bed fusion (L-PBF) of Ti-6Al-4V titanium alloy. J Manuf Process 2023;94:20–34. https://doi.org/10.1016/j.jmapro.2023.03.055.

[4] Ullah R, Lian J, Akmal J, Wu J, Niemi E. Prediction and validation of melt pool dimensions and geometric distortions of additively manufactured AlSi10Mg. Int J Adv Manuf Technol 2023;126:3593–613. https://doi.org/10.1007/s00170-023-11264-w.

[5] Huang H, Wang Y, Chen J, Feng Z. A comparative study of layer heating and continuous heating methods on prediction accuracy of residual stresses in selective laser melted tube samples. Integr Mater Manuf Innov 2021:218–30. https://doi.org/10.1007/s40192-021-00217-4.

[6] Marcotte1 J-P, Kabanemi1 K, Molavi-Zarandi1 M, Ilinca1 F, Cagnone J-S. Development of a thermomechanical model for prediction of residual stress during laser powder-bed fusion: evaluation of inherent strain approach. In: 14th World Congress in Computational Mechanics (WCCM); 2021. p. 11–5. https://doi.org/10.23967/wccm-eccomas.2020.120.

[7] Bayat M, De Baere D, Mohanty S, Hattel JH. Multi-scale multiphysics simulation of metal L-PBF AM process and subsequent mechanical analysis. In: The 12th International Seminar Numerical Analysis of Weldability - Schloss Seggau, Seggauberg, Austria. vol. 12; 2018. https://doi.org/10.3217/978-3-85125-615-4-55.

[8] Nagaraja KM, Li W, Qian D, Vasudevan V, Pyun Y, Lu H. Multiphysics modeling of in situ integration of directed energy deposition with ultrasonic nanocrystal surface modification. Int J Adv Manuf Technol 2022;120:5299–310. https://doi.org/10.1007/s00170-022-09082-7.

[9] Kaess M, Werz M, Weihe S. Residual stress formation mechanisms in laser powder bed fusion—a numerical evaluation. Materials 2023;16. https://doi.org/10.3390/ma16062321.

[10] Balbaa M, Elbestawi M. Multi-scale modeling of residual stresses evolution in laser powder bed fusion of inconel 625. J Manuf Mater Process 2022:6. https://doi.org/10.3390/jmmp6010002.

[11] Parry LA. Investigation of residual stress in selective laser melting. 2017.

[12] Huang H, Wang Y, Chen J, Feng Z. An efficient numerical model for predicting residual stress and strain in parts manufactured by laser powder bed fusion. J Phys Mater 2021:4. https://doi.org/10.1088/2515-7639/ac09d5.

[13] Pant P, Sjöström S, Simonsson K, Moverare J, Proper S, Hosseini S, et al. A simplified layer-by-layer model for prediction of residual stress distribution in additively manufactured parts. Metals (Basel) 2021:11. https://doi.org/10.3390/met11060861.

[14] Chen Q. Multiscale process modeling of residual deformation and defect formation for laser powder bed fusion additive manufacturing. 2022.

[15] Soundararajan B, Sofia D, Barletta D, Poletto M. Review on modeling techniques for powder bed fusion processes based on physical principles. Addit Manuf 2021: 47. https://doi.org/10.1016/j.addma.2021.102336.

[16] Mathews R, Nagaraja KM, Zhang R, Sunny S, Yu H, Marais D, et al. Temporally continuous thermofluidic–thermomechanical modeling framework for metal additive manufacturing. Int J Mech Sci 2023;254. https://doi.org/10.1016/j.ijmecsci.2023.108424.

[17] Flow Science. Inc. FLOW-3D 2022 R1 n.d. https://www.flow3d.com/products/flow-3d/flow-3d-2022r1/ (accessed March 7, 2022).

[18] Alphonso WE, Baier M, Carmignato S, Hattel JH, Bayat M. On the possibility of doing reduced order, thermo-fluid modelling of laser powder bed fusion (L-PBF) – assessment of the importance of recoil pressure and surface tension. J Manuf Process 2023;94:564–77. https://doi.org/10.1016/j.jmapro.2023.03.040.

[19] Fotovvati B, Chou K. Multi-layer thermo-fluid modeling of powder bed fusion (PBF) process. J Manuf Process 2022;83:203–11. https://doi.org/10.1016/j.jmapro.2022.09.003.

[20] Dassault Systèmes. ABAQUS 2021. https://www.3ds.com/products-services/simulia/products/abaqus/; 2021 (accessed March 7, 2022).

[21] Yang X, Barrett RA, Tong M, Harrison NM, Leen SB. Towards a process-structure model for Ti-6Al-4V during additive manufacturing. J Manuf Process 2021;61: 428–39. https://doi.org/10.1016/j.jmapro.2020.11.033.

[22] Jimenez Abarca M, Darabi R, de Sa JC, Parente M, Reis A. Multi-scale modelling modeling for prediction of residual stress and distortion in Ti-6Al-4V Ti–6Al–4V semi-circular thin-walled parts additively manufactured by laser powder bed fusion (LPBF). Thin-Walled Struct 2023;182. https://doi.org/10.1016/j.tws.2022.110151.

[23] Zhang Y, Outeiro JC, Mabrouki T. On the selection of Johnson-Cook constitutive model parameters for Ti-6Al-4V using three types of numerical models of orthogonal cutting. Procedia CIRP 2015;31:112–7. https://doi.org/10.1016/j.procir.2015.03.052. Elsevier B.V.

[24] Yadroitsava I, Els J, Booysen G, Yadroitsev I. Peculiarities of single track formation from TI6Al4V alloy at different laser power densities by selective laser melting. S Afr J Ind Eng 2015;26:86–95. https://doi.org/10.7166/26-3-1185.